Materials Reports: Solidwaste and Ecomaterials
Journal Homepage: www.sciopen.com/journal/3078-4093

Original Research Report

Optimizing the rheology, microstructure and carbon sequestering performance of alkali activated material incorporating acetic acid modified fly ash

Binbin Huo[1, 2], Jixiong Zhang[1, 3, *], Nan Zhou[1, 2], Meng Li[2], Qiang Guo[1], Manti Tan[1], Yifan Zhang[1], Xiao Wang[4, *]

[1] MOE Key Laboratory of Deep Coal Resource Mining, School of Mines, China University of Mining and Technology, Xuzhou 221116, China

[2] State Key Laboratory for Fine Exploration and Intelligent Development of Coal Resources, China University of Mining and Technology, Xuzhou 221116, China

[3] Jiangsu Key Laboratory for Clean Utilization of Carbon Resources, China University of Mining and Technology, Xuzhou 221116, China

[4] School of Environmental Engineering, Xuzhou University of Technology, Xuzhou 221008, China

*Corresponding Authors: J. Zhang (cumtzjxiong@163.com); X. Wang (x.wang@xzit.edu.cn)

Graphical abstract

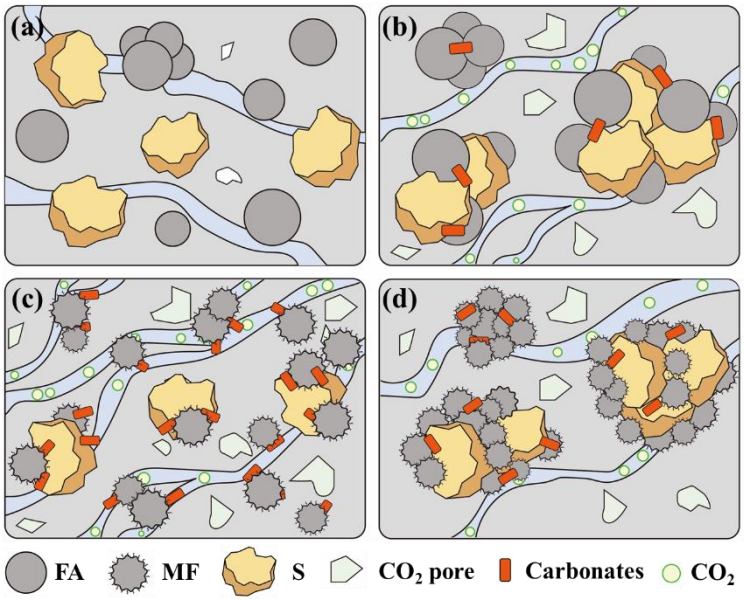

Fig. AFB microstructure and CO_2 sequestration schematic: (a) AFB0(R), (b) AFB0(C), (c) AFB2(C) and (d) AFB4(C).

Citation: B. Huo, J. Zhang, N. Zhou, et al. Optimizing the rheology, microstructure and carbon sequestering performance of alkali activated material incorporating acetic acid modified fly ash. *Materials Reports: Solidwaste and Ecomaterials*, **2026**, 2: 9520035. https://doi.org/10.26599/MRSE.2026.9520035.
Received 08 June 2026; Received in revised form 09 September 2026; Accepted 13 September 2026

Abstract: The integration of CO_2 sequestration with alkali activated fly ash (FA) backfill slurry presents a promising strategy for simultaneous resource utilization of industrial waste and carbon capture. However, the efficiency of this process is often constrained by the inherently poor reactivity of FA and rheology of FA based slurry. This investigation applies acetic acid (AA) to modify FA in order to improve the CO_2 sequestration and rheology properties of alkali activated FA based backfill (AFB) slurry. Results reveal that a non-monotonic relationship between AA dosage and CO_2 sequestration capacity of AFB, characterized by an initial increase followed by a decline. At 1 wt.% AA, the material achieves its maximum CO_2 uptake of 1.28% and peak yield stress (10.54 Pa). This improvement originates from AA-driven surface modification, resulting in finer particles and higher reactivity compared to that of the control group. Furthermore, AA adsorbs onto FA surface functions as a lubricant and dispersant, thereby improving slurry rheology. Carbon life cycle assessment indicates that AFB employing 1 wt.% AA modified FA reduces total emissions by 69.52 kg/t compared to that of the unmodified reference, underscoring the potential of this strategy for achieving negative carbon emissions in mining backfill applications.

Keywords: fly ash; alkali activated material; CO_2 sequestration; modification; carbon footprint

1. Introduction

Fly ash (FA), a kind of aluminosilicate waste from coal fired power plants, hit a global annual output of 1280 Mt in 2025, with China producing over 748 Mt annually. Untreated FA stockpiles can trigger land and water pollution [1]. The mainstream applications of FA include cement admixtures, flue gas sorbents and mine backfill [2]. Among these, alkali activated FA backfill with in-situ CO_2 mineralization stands as a feasible pathway for large scale disposal and carbon neutrality [3]. However, two critical drawbacks block its low carbon deployment. First, dense inert glass phases wrap Ca^{2+} and Mg^{2+} in raw FA, slowing ions dissolution and lowering early carbon sequestration efficiency of backfill slurry [4]. Second, $CaCO_3$ precipitates formed during CO_2 mineralization fill particle gaps and aggravate flocculation, drastically worsening slurry flowability [5]. The dual limits of weak early mineralization and degraded post carbonation fluidity hinder widespread engineering application of carbon negative FA backfill.

To improve the pozzolanic reactivity of FA, three representative activation approaches have been proposed, such as mechanical milling, alkali activation, and integrated mechanochemical modification. Hamada et al. [6] reported that wet ball milling for 8 h reduced FA median particle size from 29403 nm to 543 nm, with a reduction rate of 98.2%. Meanwhile, the BET surface area of FA elevated from 1.624 m^2/g to 6.772 m^2/g. The wet ball milling breaks inert glass phases and substantially improves pozzolanic reactivity of FA. For chemical activation, Li et al. [7] found that 0.5 M NaOH activator achieved a 28 d compressive strength of 7.18 MPa, 56.8% higher than that of the samples with 0.1

M NaOH under identical curing conditions. In terms of mechanochemical coupling approach, Zhao et al. [8] combined 60 min milling with halogen salt modification. The cured material based on treated FA achieved 12.56 MPa at 28 d, representing a 74.9% improvement than unmodified samples. Distinct from mechanical and composite alkali activation routes, Huo et al. [9] proposed dry phosphoric acid modification for steel slag. The acid treatment etches steel slag particles to form abundant pore structures and accelerates hydration reactions, effectively elevating the inherent reactivity of raw steel slag particles. Furthermore, relevant studies provide solid experimental data on acetic acid leaching of calcium bearing residues. Rong et al. [10] fabricated steel slag derived CO_2 sorbents using 1 mol/L acetic acid at 60 °C with a slag-acid ratio of 1:15 for 2 h. The sorbent achieved a 0.38 g/g carbon dioxide uptake after 15 cycles, and 40 volume percent steam in carbonation improved adsorption capacity by 53%. Bao et al. [11] proposed an acetic acid–tributyl phosphate (TBP) biphasic leaching system for steel slag. At an acid-solid mass ratio of 0.5–1.0 g/g, calcium and magnesium leaching rates reached 75% and 35% with nearly 100% selectivity over iron and aluminum. Although all these approaches effectively accelerate alkaline earth metal ion dissolution and enhance mineralization capacity, these modifications impair the fresh state flowability of blended slurries for increased specific surface area [12].

To alleviate rheological degradation of cementitious pastes after CO_2 mineralization, multiple approaches have been reported. The primary approaches include increasing the water to binder ratio, incorporating polycarboxylate ether (PCE) superplasticizers, optimizing alkali activator modulus and aggregate gradation. Increasing the water to binder ratio is a straightforward way to mitigate carbonate induced flocculation. Zhao et al. [13] reported that raising free water reduced slurry yield stress from 59.33 Pa to 3.82 Pa, yet excessive water expanded capillary pores and reduced the 28 d compressive strength by 41.6% after carbonation curing. Zhang et al. [14] confirmed that 1.2 wt.% PCE cut plastic viscosity by 58.2% due to superplasticizers disperse solid particles via steric hindrance. However, $CaCO_3$ precipitates continuously consumed PCE during mineralization, requiring higher dosages and engineering cost. Adjusting activator modulus balances gel formation and fluidity. Pan et al. [15] found that a low sodium silicate modulus slowed gel flocculation, but suppressed Ca^{2+} release and early carbon sequestration efficiency. Optimizing aggregate gradation helps to reduce internal friction. Cao et al. [16] adopted an aggregate fractal dimension of 2.65 to fill gaps between carbonate crystals, lowering the thixotropic loop area by 32.4%. However, this approach limited FA dosage, and thus reduced waste utilization and carbon capture capacity. All above approaches have certain drawbacks, such as higher water to binder ratios impair matrix strength, while superplasticizers increase material expenses. A method that can simultaneously boost FA pozzolanic reactivity and sustain stable flowability of carbonated backfill slurry calls for further exploration.

The previous study has demonstrated that pretreatment of coal gasification slag using acetic acid (AA) can improve the workability of backfill slurry [17]. To optimize the CO_2 sequestration efficiency

and rheological performance, AA modified alkali activated FA based backfill (AFB) was prepared through systematic AA treatment of FA precursors. This investigation employs a variety of characterization methods, including X-ray diffraction (XRD), thermogravimetric analysis (TG/DTG), Brunauer Emmett Teller (BET) surface area measurements, and scanning electron microscopy (SEM), to elucidate the fundamental mechanism governing CO_2 sequestration and rheological modification in AFB system. The findings provide key insights for developing sustainable backfill technologies that address both carbon neutrality and large-scale FA utilization in mining applications.

2. Materials and methods

2.1. Raw materials

The experimental materials comprise FA sourced from Shaanxi Binzhou Electric Power Co. Ltd. and slag (S) obtained from Northwest Mining Co. Ltd. Particle size distribution analysis (Fig. 1), conducted by laser diffraction (Mastersizer 3000, Malvern Panalytical), revealed median particle diameters (D_{50}) of 19.01 μm for FA and 2.21 μm for S, with corresponding D_{90} values of 51.19 μm and 9.34 μm, respectively. X-ray fluorescence (Axios mAX, PANalytical) and X-ray diffraction (Empyrean, Malvern Panalytical) were employed to characterize the chemical and mineral compositions (Table 1, Fig. 2) of FA and S. Glacial acetic acid was utilized (AA, ≥99.5% purity) as a chemical modifier. Alkali activation was achieved using a sodium silicate solution (water glass, Na_2SiO_3; modulus Ms = 1.4, where Ms represents the SiO_2/Na_2O molar ratio) combined with sodium hydroxide (NaOH), yielding a final Na_2O content of 4 wt.%. High purity CO_2 (>99%) was supplied by Xuzhou Jinhong Gas Co., Ltd. for carbonation experiment.

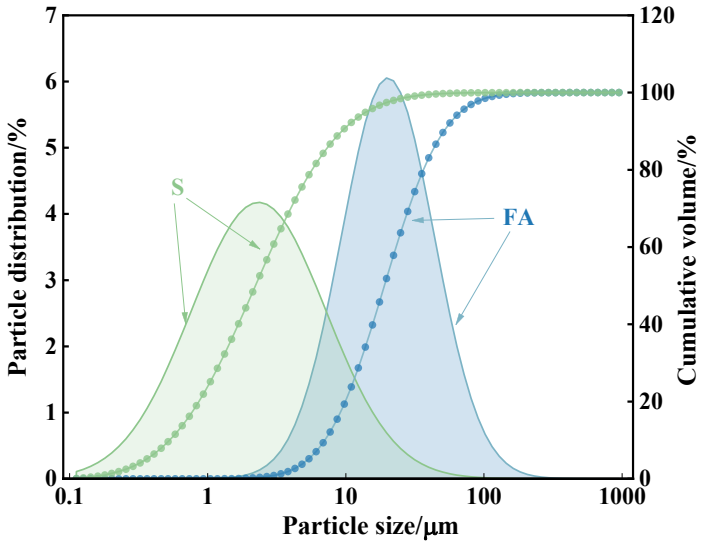

Fig. 1. Particle size distribution of FA and S.

Table 1. Chemical composition of FA and S, wt.%.

Composition	SiO_2	Al_2O_3	Fe_2O_3	CaO	K_2O	MgO	Na_2O	TiO_2	SO_3
FA	51.55	33.90	3.60	4.05	1.95	1.86	0.52	1.32	1.25
S	30.48	17.03	0.58	33.47	0.47	14.44	0.37	0.79	2.37

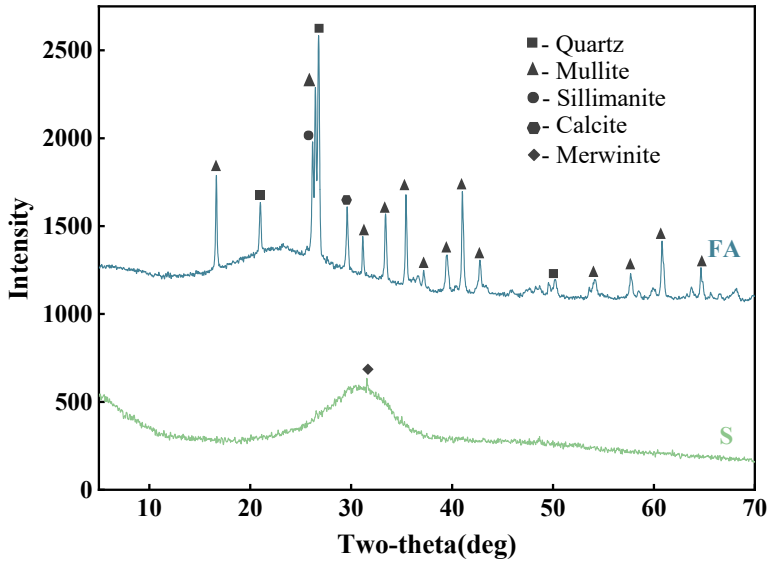

Fig. 2. XRD patterns of FA and S.

2.2. Sample preparation

2.2.1. Chemical modification

The chemical modification of FA adopted an established protocol [17], comprising three key steps:

(1) Pre-dispersion: 100 g of FA was dispersed in a 250 mL conical flask with stirring (360 rpm, 10 min) to break particle agglomerates.

(2) Acid modification: as specified in Table 2, AA of varying dosage was added dropwise (2-5 min total addition time), with >1 s intervals between drops to ensure homogeneous distribution throughout the FA.

(3) Mechanical activation: Alumina (corundum) grinding ball with a mass ratio of 5 mm:10 mm:15 mm = 5:2:3 was mixed. The mass ratio of grinding balls to FA powder (ball to powder ratio) was set at 5:1 [18]. The AA-treated mixture was subjected to ball milling (520 rpm, 60 min), yielding the final modified fly ash (MF).

Table 2. Mixing proportions of modified FA samples.

No.	MF0	MF1	MF2	MF4	MF6
AA/g	0	1	2	4	6
FA/g	100	100	100	100	100

2.2.2. Carbonation process

The carbonation reaction was conducted in a custom-designed system (Fig. 3). Precursor materials were homogenized according to the formulations detailed in Table 3 [19] and transferred to the reaction vessel. The internal relative humidity inside the pressurized carbonation reactor was maintained at RH=95 %, consistent with the humidity condition of fresh backfill slurry. Prior to carbonation, the reactor was purged with CO_2 to eliminate atmospheric gases, followed by sealing of the outlet valve. Reaction conditions were maintained at 500 rpm agitation speed, 0.4 MPa pressure, and 30 °C for 30 min [20, 21].

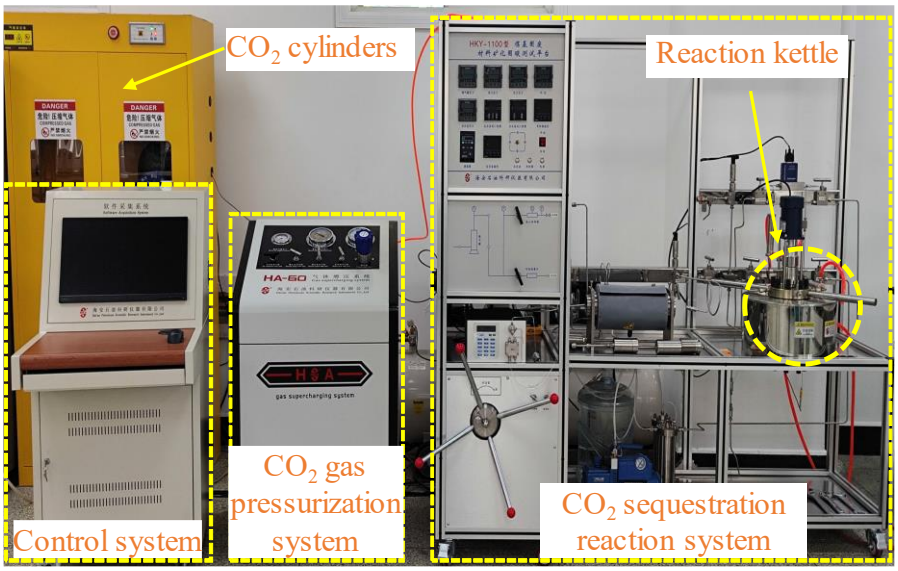

Fig. 3. Carbonation reaction device.

Table 3. Mixing proportions of the slurry.

No.	MF/g	S/g	Water/Binder	Alkali activator (Na_2O equivalent, wt.%)
AFB0(R)	70-MF0	30	0.8	4
AFB0(C)	70-MF0	30	0.8	4
AFB1(C)	70-MF1	30	0.8	4
AFB2(C)	70-MF2	30	0.8	4
AFB4(C)	70-MF4	30	0.8	4
AFB6(C)	70-MF6	30	0.8	4

*MF represents modified FA, R represents uncarbonized group, C represents carbonized group. The value in the "Alkali activator" column stands for the Na_2O equivalent percentage relative to binder.

2.3. Test methods

2.3.1. CO_2 sequestration capacity

The CO_2 sequestration capacity of the AFB was quantitatively determined through gravimetric analysis using a precision analytical balance (Mettler Toledo XSR205, ±0.0001 g measurement uncertainty). To ensure statistical reliability, all measurements were performed in triplicate, with results averaged and standard deviation calculated for error-bar plotting to minimize experimental error. The total CO_2 sequestration capacity (C, wt.%) was calculated according to Equation (1):

$$CO_{2\ uptake}(Total, wt.\%) = \frac{m_1 - m_0}{m_0} \times 100\% \quad (1)$$

Where, m_0 is the mass of the sample before carbonization, and m_1 is the mass of the sample after carbonization.

2.3.2. Rheology test

Rheological characterization of the AFB was performed using an Anton Paar MCR 72 rheometer (Austria) equipped with a four-bladed vane rotor (ST22-4V-40 geometry: 22 mm diameter, 40 mm height). Prior to test, the homogenized slurry was transferred to a cylindrical measurement cell (110 mm diameter × 120 mm height). The vane rotor was precisely positioned at the geometric center of the container using the instrument's automated alignment system, with an immersion depth maintaining 20 mm clearance between the rotor tip and slurry surface. This standardized configuration minimizes wall slip effects and ensures measurement reproducibility by eliminating boundary-induced artifacts [22].

Rheological tests followed modified standard protocols [17]. First, slurries were pre-sheared at 60 s^{-1} for 60 s and rested for 30 s to stabilize internal structures. Afterwards, shear rates were swept from 0 to 120 s^{-1} (forward and backward), with 120 sampling points collected every 3 s to record complete flow curves.

2.3.3. X-ray diffraction (XRD)

First, a pretreatment of samples in anhydrous ethanol for 24 h was conducted, with solvent replacement every 12 h to maintain dehydration efficiency. Then, samples were vacuum-dried at 45 °C for 24 h and subsequently pulverized to 200 mesh particle size. Phase composition analysis was performed using a Rigaku Smart Lab SE X-ray diffractometer (Cu Kα radiation, λ = 1.5406 Å). Diffraction patterns were acquired over a 2θ range of 5-70° with a scanning rate of 5°/min.

2.3.4. Thermogravimetric analysis (TGA)

TGA was conducted using 3 d cured samples on a Netzsch TG 209 F3 Tarsus thermogravimetric analyzer (Germany). Approximately 10 mg of sample was loaded into a platinum crucible under nitrogen atmosphere (flow rate: 20 mL/min). Measurements were performed with a temperature ramp of 10 °C/min from 30 to 1000 °C, utilizing embedded high-precision microbalance (sensitivity: 0.1 μg; accuracy: ±0.01% of measured value).

2.3.5. Fourier transform infrared (FT-IR) spectroscopy

FT-IR analysis was performed using a Thermo Fisher Scientific Nicolet iS20 spectrometer (USA) to characterize the chemical composition of modified FA. Sample preparation involved homogenizing approximately 1-2 mg of material with 200 mg of spectroscopic-grade KBr (1:100-200 mass ratio), followed by pellet formation under 30 MPa pressure. Spectra were acquired in transmission mode across the 400-4000 cm^{-1} range with 4 cm^{-1} resolution and 32 scans to ensure optimal signal-to-noise ratio.

2.3.6. Nitrogen adsorption-desorption isotherms

The specific surface area and pore structure characteristics were determined by nitrogen physisorption measurements using a Micromeritics ASAP 2460 analyzer (USA). Samples were degassed under vacuum at 120 °C for 12 h prior to analysis. Nitrogen adsorption-desorption isotherms were acquired at 77 K (liquid nitrogen bath temperature) over a relative pressure (P/P_0) range of 0.05-0.995. The Brunauer-Emmett-Teller (BET) method was employed to calculate specific surface area from the adsorption data in the linear P/P_0 range of 0.05-0.30, while pore size distribution was derived from the desorption branch using the Barrett-Joyner-Halenda (BJH) model.

2.3.7. Optical microscope

The morphological evolution of cluster structures in AFB was investigated using optical microscopy (Leica DM500, Germany). Prior to imaging, samples were dispersed with deionized water at 1:200 mass ratio to ensure optimal particle dispersion and resolution. Bright-field images were acquired at 100× magnification under standardized illumination conditions to enable quantitative comparison of microstructural features.

2.3.8. Morphology and microstructure

Microstructural characterization was performed using a field-emission scanning electron microscope (FE-SEM, Gemini SEM 300, ZEISS, Germany) at an accelerating voltage of 20 kV. Samples were sputter-coated with a 10 nm gold-palladium layer (Quorum Q150T ES) to enhance surface conductivity prior to imaging. Secondary electron images were acquired under high vacuum conditions with working distances optimized between 5-10 mm to achieve optimal resolution.

3. Results

3.1. Effect of AA-modified FA on CO_2 sequestration and rheology of AFB

3.1.1. Effect of AA-modified FA on CO_2 sequestration of AFB

The CO_2 sequestration capacity of AFB determined by the analytical gravimetric method is presented in Fig. 4. With AA dosage increases, the CO_2 sequestration efficiency of AFB initially increases and then decreases, reaching a maximum value of 1.28% for AFB1(C) at an AA dosage of 1 wt.%. Notably, AFB1(C) exhibits a 256% enhancement in CO_2 sequestration compared to that of the AFB0(C). This trend can be attributed to two factors. First, AA modification decreases the particle size of FA and increases pore volume, thereby enhancing the specific surface area and improving CO_2 adsorption capacity. Second, AA reacts with FA to form calcium acetate, promoting Ca^{2+} leaching from FA particles and facilitating CO_2-Ca^{2+} reactions. AA enhances chemical mineralization via sustained Ca^{2+} complex leaching and cyclic mineralization reaction. AA breaks FA aluminosilicate glass to release Ca^{2+}. Acetate binds Ca^{2+} into soluble complexes, preventing passivating $Ca(OH)_2$ precipitation under strong alkali [23, 24]. These findings align with previous work by Guo et al. [17]. However, when the AA dosage exceeds 1 wt.%, the CO_2 sequestration capacity of AFB decreases. This reduction arises from excessive calcium acetate formation, which acts as inter-particle bridges, reducing the specific surface area and consequently decreasing CO_2 sequestration performance [9].

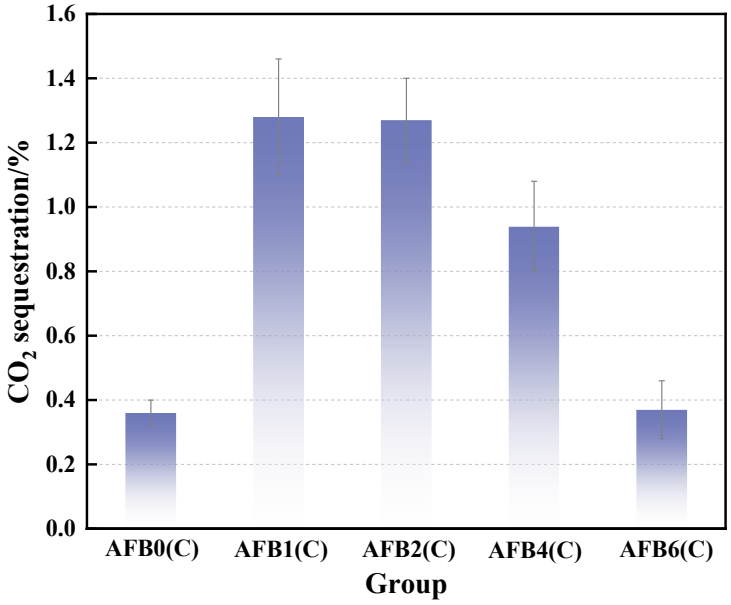

Fig. 4. Carbonation of AFB under different AA dosages.

3.1.2. Effect of AA-modified FA on rheology of AFB

The relationship between shear stress and shear rate is presented in Fig. 5(a). Notably, AFB0(C) exhibits higher shear stress than AFB0(R) at equivalent shear rates, attributing to the surface deposition of calcium carbonate after CO_2 sequestration. This deposition adversely affects particle interactions, leading to degraded slurry rheology [25]. After incorporation of AA-modified FA, the shear stress of AFB displays a non-monotonic dependence on AA dosage. The minimum shear stress occurs at an AA dosage of 2 wt.%, suggesting an optimal modification threshold beyond which rheological performance deteriorates.

Fig. 5(b) illustrates the apparent viscosity as a function of shear rate. The apparent viscosity of slurry with varying AA dosage exhibits a pronounced shear-thinning behavior, decreasing sharply with increasing shear rate before stabilizing at shear rates above 55 s^{-1}. This rheological behavior arises from the dynamic evolution of the internal flocculation network under shear. When subjected to external forces, the network structure undergoes continuous breakdown due to shear-induced deformation, while simultaneously reforming through particle interactions [26]. The apparent viscosity reaches a plateau when the rates of structure breakdown and reformation achieve dynamic equilibrium.

To further analyze the yield stress and plastic viscosity of AFB, the Herschel-Bulkley (H-B) model is used. The fitting coefficient R^2 is greater than 0.99, showing a good fitting effect. The H-B model can be described as:

$$\tau=\tau_0+\eta\gamma^n \quad (2)$$

Where, τ is shear stress, Pa, τ_0 is yield stress, Pa, η is plastic viscosity, Pa·s, n is rheological index. When n<1, the slurry has shear thinning characteristics; when n>1, the slurry has shear

thickening characteristics; when n=1, the slurry is a Bingham fluid. The rheological parameters of AFB after H-B fitting are shown in Table 4. Herein n<1 also indicates that the slurry has shear thinning characteristics [27].

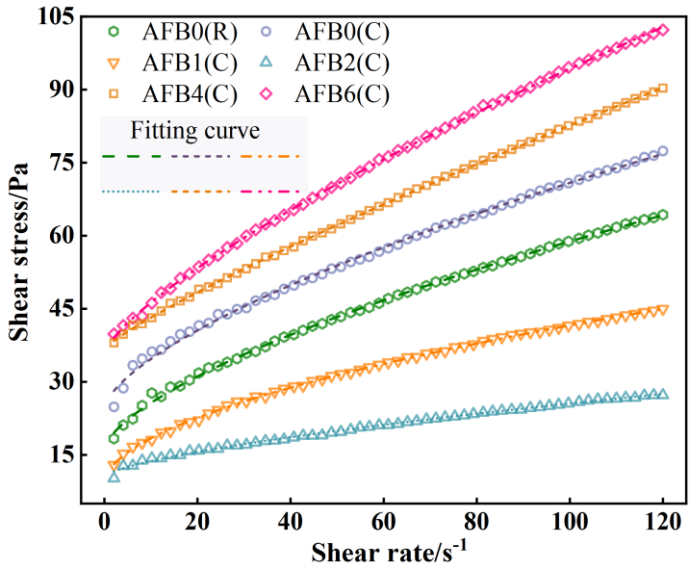

(a)

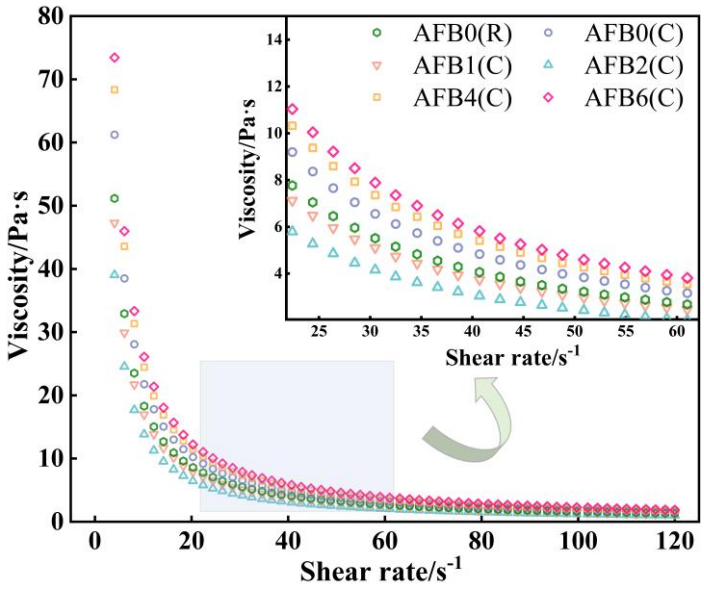

(b)

Fig. 5. (a) Shear stress and (b) viscosity versus shear rate of AFB at varying AA dosages.

Table 4. Rheological model of AFB at varying AA dosages.

No.	Rheological model	Fitting results	τ_0 /Pa	η / Pa·s	*n*	R^2
AFB0(R)	H-B	$\tau=16.18+0.96\gamma^{0.65}$	16.18	0.96	0.65	0.9993
AFB0(C)		$\tau=24.63+2.19\gamma^{0.66}$	24.63	2.19	0.66	0.9987
AFB1(C)		$\tau=10.54+1.84\gamma^{0.55}$	10.54	1.84	0.55	0.9992
AFB2(C)		$\tau=9.28+0.67\gamma^{0.64}$	9.28	0.67	0.64	0.9994
AFB4(C)		$\tau=35.92+1.62\gamma^{0.85}$	35.92	1.62	0.85	0.9989
AFB6(C)		$\tau=36.75+1.84\gamma^{0.75}$	36.75	1.84	0.75	0.9994

Fig.6 shows yield stress (threshold for plastic flow [28]) and plastic viscosity (flow resistance [29]) against AA dosage. Carbonized AFB0(C) has higher yield stress (24.63 Pa vs. 16.18 Pa) and plastic viscosity (2.19 Pa·s vs. 0.96 Pa·s) than uncarbonized AFB0(R). This deterioration can be explained from two aspects, the exothermic carbonation evaporates free water and weakens interparticle water lubrication [30], and precipitated carbonates cover particle surfaces to hinder flow [31].

After incorporation of AA-modified FA, the yield stress and plastic viscosity demonstrate a non-monotonic dependence on AA dosage. At 2 wt.% AA dosage, the carbonized slurry AFB2(C) shows 62% lower yield stress (9.28 Pa vs. 24.63 Pa) and 69% lower plastic viscosity (0.67 Pa·s vs. 2.19 Pa·s) compared to that of the AFB0(C). Its thixotropic hysteresis area achieves a minimum of 144.05 Pa/s, an 80.40% drop compared to that of the AA-free carbonized sample. Optical microscopy (Fig.12) verifies AFB2(C) has evenly dispersed particles free of large agglomerates, matching its low macroscopic flow resistance. Multiple rheological indicators collectively prove 2 wt.% AA is optimal for slurry fluidity, distinct from the 1 wt.% AA dosage that maximizes CO_2 uptake. Such flow improvement originates from surface-adsorbed organic AA molecules that lubricate particles [17]. However, exceeding this optimal dosage leads to a remarkable increase in both parameters due to excessive particle size reduction and corresponding specific surface area expansion of FA particles [32].

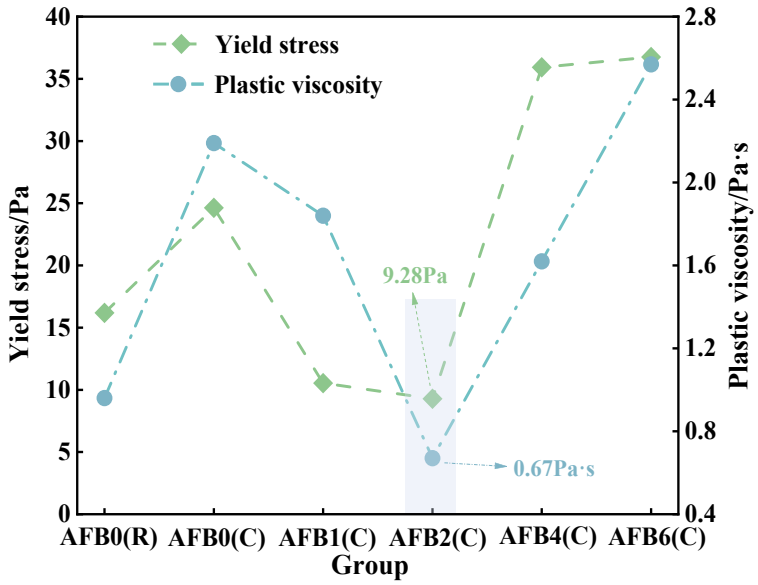

Fig. 6. Effect of AA dosages on yield stress and viscosity of AFB.

Fig.7 presents the hysteresis loops of AFB containing FA modified with varying AA dosage. The thixotropic behavior of the slurry is quantified by the integrated area between the ascending and descending curves, reflecting the energy required to break down the flocculated structures that impede flow [33]. While all formulations exhibit thixotropic behavior, the magnitude of the hysteresis area and consequently the degree of thixotropy show significant variation with AA dosage. This dependence arises from AA modification to the slurry's internal structure, which directly influence the formation and stability of flow resistant flocculent network.

Fig. 8 quantifies the hysteresis loop area for different formulations. The AFB0(C) system exhibits a 278.18 Pa/s increase in hysteresis area relative to AFB0(R), reflecting increased system complexity due to carbonate product formation. Notably, the hysteresis area demonstrates a non-monotonic dependence on AA dosage. The minimum hysteresis area (144.05 Pa/s, representing an 80.40% reduction compared to that of the AA-free system) occurs at 2 wt.% AA dosage, corresponding to maximal structural simplicity. Further AA addition leads to renewed system complexity, as evidenced by the rapidly expanding hysteresis area.

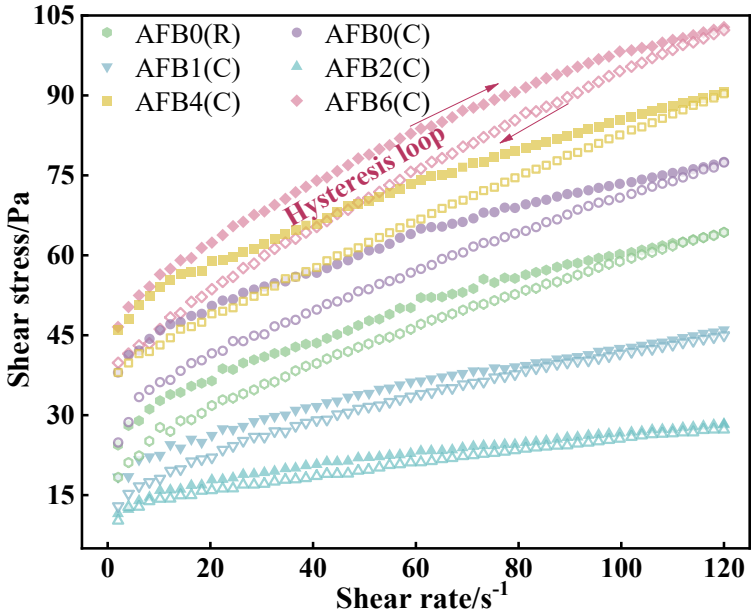

Fig. 7. Effect of AA dosages on the thixotropic loop of AFB.

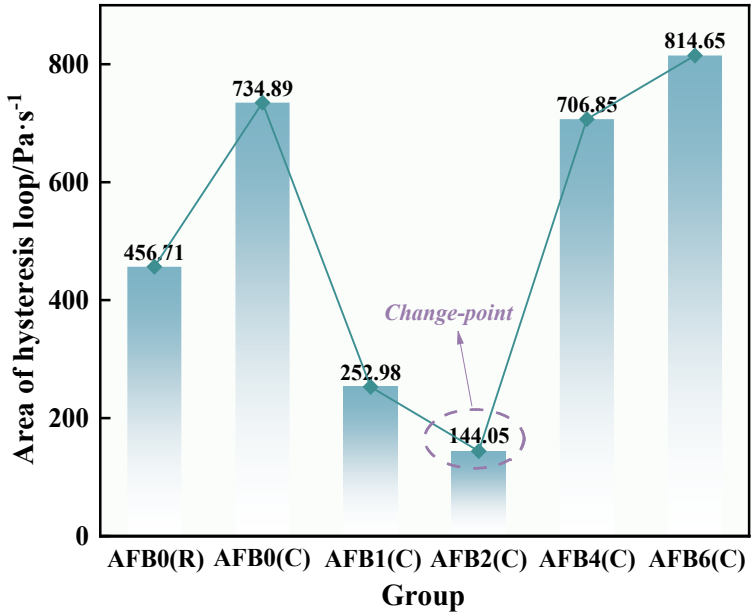

Fig. 8. Effect of AA dosages on the thixotropic loop area of AFB.

3.2. Effect of AA-modified FA on the composition and microstructure of AFB

3.2.1. XRD analysis

Fig. 9 presents the XRD patterns of the investigated samples. The diffraction analysis reveals three primary crystalline phases: quartz (SiO_2), mullite ($3Al_2O_3{\cdot}2SiO_2$), and calcite ($CaCO_3$) [34]. Notably, the calcite peak intensity in AFB0(C) shows marked enhancement relative to AFB0(R), confirming successful carbon sequestration. With increasing AA dosage up to 2 wt.%, it was observed a progressive intensification of calcium carbonate diffraction peaks, consistent with enhanced calcium

ion leaching from FA and subsequent carbonation. This trend reverses at higher AA concentrations (>2 wt.%), where excessive calcium acetate formation promotes interparticle bridging [9], ultimately decreasing both calcite formation and CO_2 sequestration efficiency.

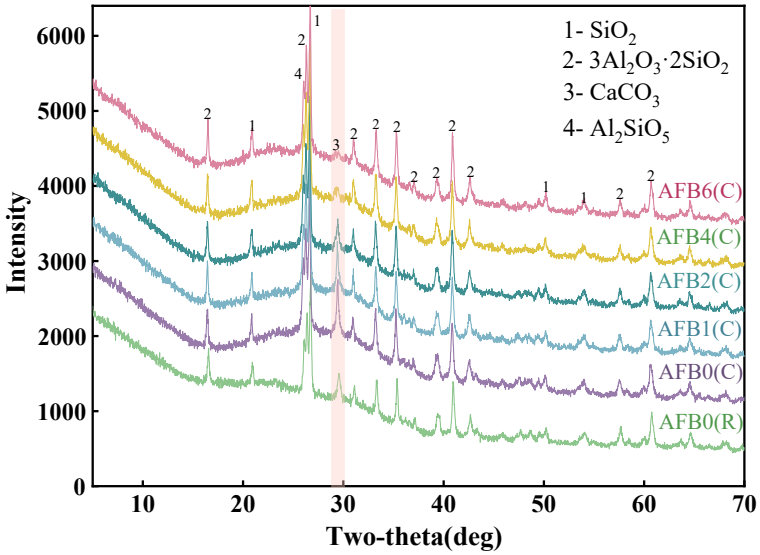

Fig. 9. XRD patterns of AFB at different AA dosages.

3.2.2. TG/DTG analysis

Fig. 10 presents the thermogravimetric (TG) and derivative thermogravimetric (DTG) curves of AFB during the temperature range of 30-1000°C. The thermal decomposition process exhibits three distinct mass loss stages. Stage I (30-200°C): Primarily attributed to dehydration of hydrated phases, including ettringite (AFt) and C-S-H gel. Stage II (350-540°C): Corresponds to dehydroxylation of crystalline hydroxides such as portlandite ($Ca(OH)_2$) and brucite ($Mg(OH)_2$). Stage III (540-950°C): Results from decarbonation of carbonate, particularly calcite ($CaCO_3$) [35, 36]. The CO_2 uptake capacity of carbonated specimens can be quantitatively determined using Equation (3).

$$W_{CO_2}(\%) = \frac{W_{540} - W_{950}}{W_0} \times 100\% \quad (3)$$

Where, W_{540} is the mass of the test sample at 540 ℃, W_{950} is the mass of the test sample at 950 ℃, and W_0 is the initial mass of the sample.

TG quantification results are presented in Table 5. Comparative analysis reveals that AFB0(C) exhibits decreased mass loss in Stages I and II but increased mass loss in Stage III compared to that of the AFB0(R). This behavior reflects the carbonation of C-S-H gel and $Ca(OH)_2$ to form carbonates. At an optimal AA dosage of 1 wt.% for CO_2 sequestration, a chemical CO_2 sequestration capacity of 0.72% is achieved, whereas the best rheological property is acquired at 2 wt.% AA dosage, the mild rheology improvement of AFB1(C) is attributed to particle surface modification by lubricating AA molecules [17]. Notably, the TG-derived CO_2 sequestration values are systematically lower than that of the values obtained in Section 3.1.1. This discrepancy arises from the dual sequestration

mechanisms in AFB systems: (1) chemical mineralization (quantified by TG) and (2) physical adsorption within the porous matrix (detected in bulk measurements but not by thermal analysis).

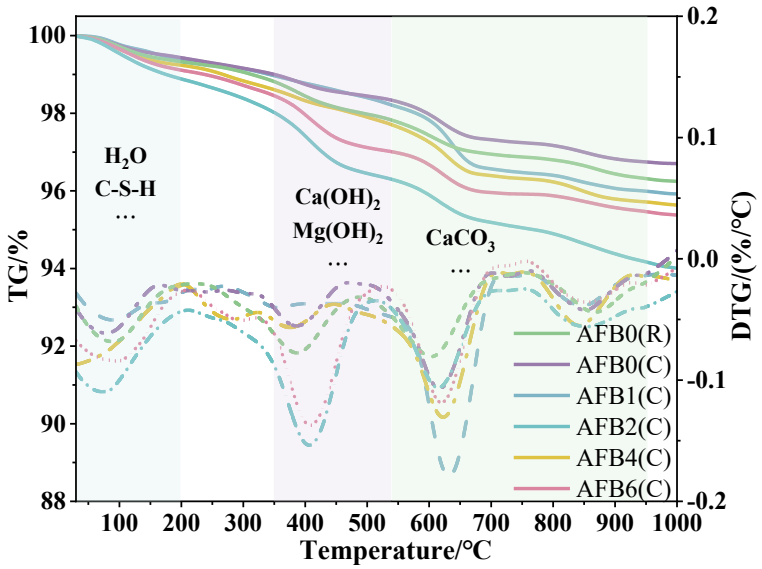

Fig. 10. TG-DTG curves of AFB at different AA dosages.

Table 5. TG quantitative statistical results (%).

Group	AFB0(R)	AFB0(C)	AFB1(C)	AFB2(C)	AFB4(C)	AFB6(C)
Stage I: 30~200℃	0.67	0.56	0.60	1.11	0.75	0.88
Stage Ⅱ: 350~540℃	0.99	0.67	0.76	1.71	0.91	1.44
Stage Ⅲ: 540~950℃	1.50	1.64	2.22	2.13	1.98	1.54
CO_2 Sequestration capacity	0	0.14	0.72	0.63	0.48	0.04

3.2.3. FTIR analysis

Fig. 11 presents the FTIR spectra of AFB with varying AA dosages. The curves in Fig. 11 reveal two characteristic vibrational modes: (1) the v_3 asymmetric stretching mode at 1420 cm^{-1} and the v_2 out-of-plane bending mode at 875 cm^{-1}, both characteristic of carbonate (CO_3^{2-}) groups in crystalline $CaCO_3$, and (2) the asymmetric Si-O-T (T=Al/Si) stretching vibration between 1030-1050 cm^{-1}, corresponding to the gehlenite ($Ca_2Al_2SiO_7$) phase [37]. Comparative analysis of the carbonate bands demonstrates enhanced CO_3^{2-} signal intensity after carbonation, confirming successful CO_2 sequestration. This observation aligns well with complementary XRD and TG-DTG analysis. Notably, the CO_3^{2-} band intensity follows a non-monotonic dependence on AA dosages, reaching maximum intensity at 1 wt.% AA dosage. This trend is also consistent with the preceding physicochemical

characterizations.

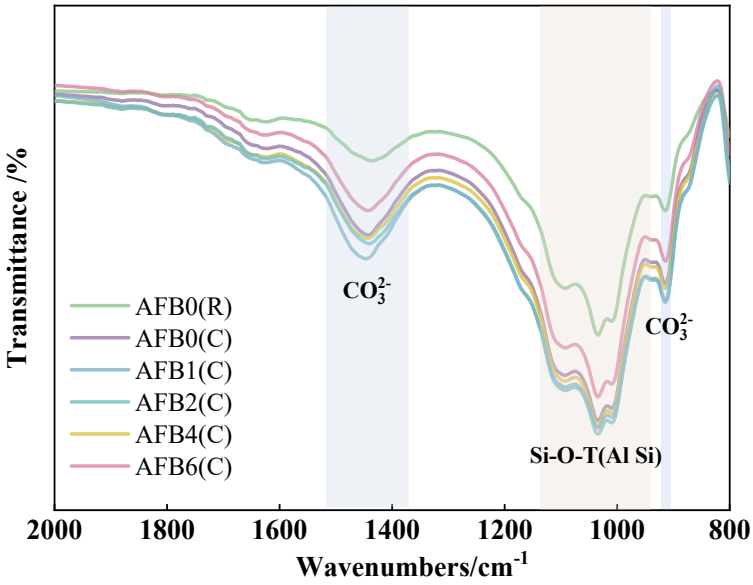

Fig. 11. FTIR spectra of AFB at different AA dosages.

3.2.4. Morphology and microstructure

Fig. 12 illustrates the evolution of cluster structures in AFB with varying AA dosages. Three distinct morphological regimes are evident. (1) The AFB0(C) sample shows significant particle agglomeration due to carbonate precipitation on particle interfaces. (2) AA modification (≤2 wt.%) effectively disperses these clusters through steric and electrostatic stabilization mechanisms. (3) Excessive AA dosage (>2 wt.%) induces renewed agglomeration as hyperhydration destabilizes the particle suspension. This non-monotonic morphological evolution directly correlates with the observed rheological performance. It demonstrates that optimal AA dosage critically balances surface modification and particle interaction dynamics.

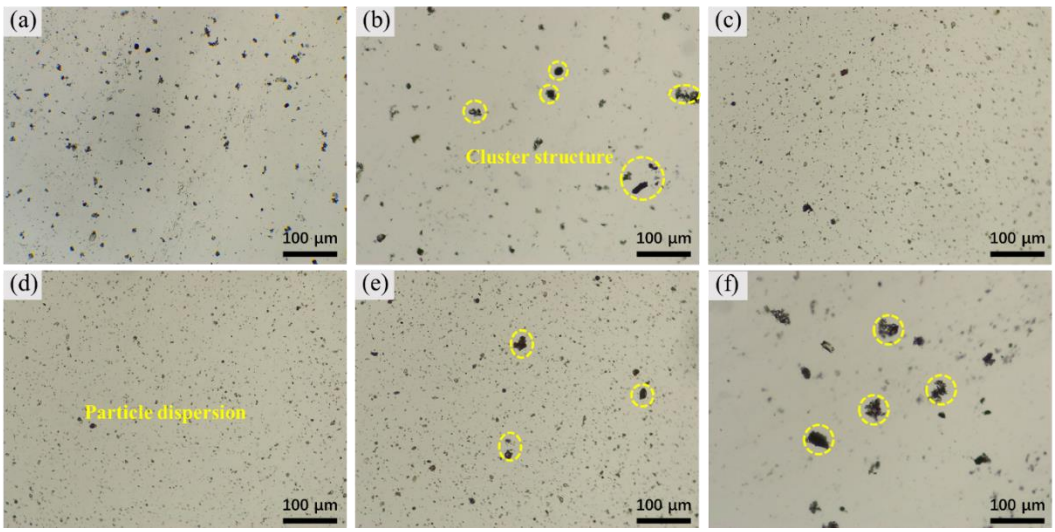

Fig. 12. The morphology of (a) AFB0(R), (b) AFB0(C), (c) AFB1(C), (d) AFB2(C), (e) AFB4(C) and (f)

AFB6(C).

Fig. 13 presents the SEM images of AFB. The microstructural examination reveals distinct spherical FA particles alongside heterogeneous hydration products. Prominent pores, cracks, and hydration phases were observed in the reference sample AFB0(R). Comparative analysis demonstrates a notable decrease in pore size for the carbonated specimen AFB0(C), attributing to the formation of calcium carbonate. Furthermore, AFB2(C) exhibits particularly enhanced matrix compactness correlated with increased $CaCO_3$ content.

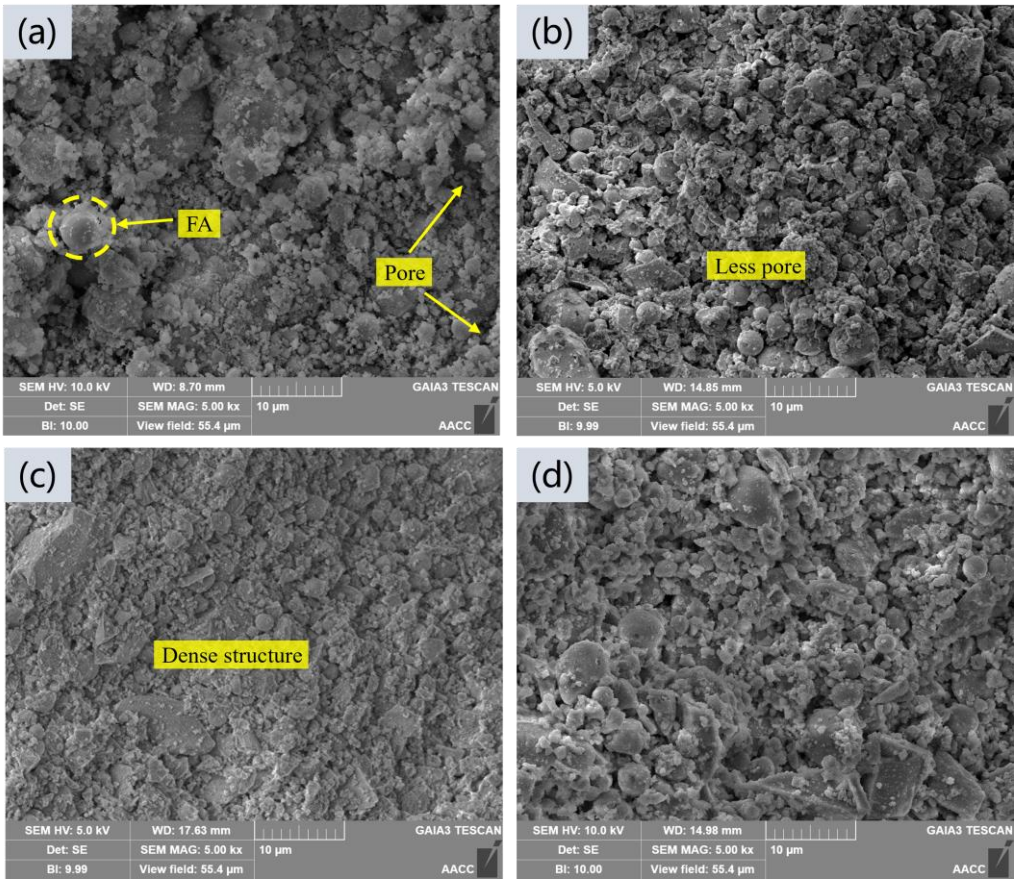

Fig. 13. SEM images of (a)AFB0(R), (b)AFB0(C), (c)AFB2(C), (d)AFB6(C).

3.3. Effect of AA modification on mineral composition and microstructure of FA

3.3.1. Mineral composition

Fig. 14 presents the XRD patterns of FA modified with varying AA dosages. $CaCO_3$ diffraction peak intensity decreases with the AA dosages. Notably, as AA dosage exceeds 2 wt.%, the $CaCO_3$ diffraction peak vanishes entirely, concomitant with the emergence of a new crystalline phase corresponding to calcium acetate ($Ca(CH_3COO)_2$). This observation confirms the reaction between $CaCO_3$ and AA, yielding $Ca(CH_3COO)_2$ as the primary product. In contrast, the quartz (SiO_2) diffraction peak remains invariant across all AA dosages, demonstrating its chemical inertness under

these modification conditions.

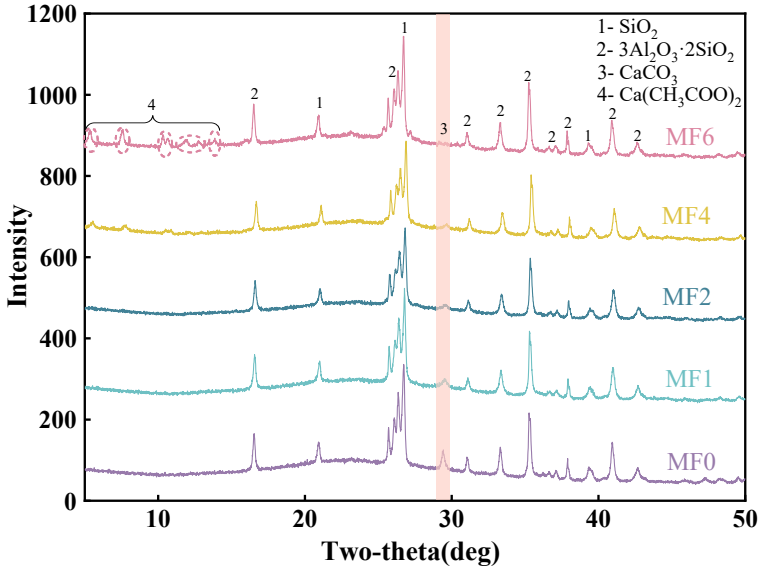

Fig. 14. XRD patterns of FA modified with different AA dosages.

3.3.2. Microscopic morphology

Fig. 15 presents SEM micrographs, elemental mapping, and statistical particle size analysis of FA before and after AA modification. The results demonstrate that AA modification significantly alters FA particle size distribution and surface morphology. Quantitative analysis of over 100 FA particles reveals that unmodified FA exhibits a maximum particle size exceeding 8 μm, with spherical particles displaying smooth surfaces. After AA modification, an obvious decrease in particle size is observed, accompanied by a marked increase in fine particle fraction. Compared to unmodified FA (MF0), MF2 exhibits a particle size distribution entirely below 8 μm and a 157% increase in particles within the 0–2 μm range.

Morphological analysis further indicates the development of surface porosity and hydration products, leading to increased surface roughness. EDS analysis confirms a progressive rise in surface content of carbon (C) and oxygen (O) with higher AA dosages, attributing to both the organic composition of AA and its reaction with surface minerals (e.g., $CaCO_3$). AA modification of FA realizes particle dispersion via electrostatic repulsion and steric lubrication at low AA dosage (1-2 wt.%) [17]. Dissociated CH_3COO^- adsorbs on FA surfaces to form homogeneous negative electrostatic layers, breaking cationic bridging between raw spherical particles and eliminating inherent agglomerates observed in MF0. Meanwhile, adsorbed AA acts as solid-liquid lubricant layers, decreasing interparticle friction and macroscopical slurry yield stress. Notably, as AA concentrations exceeds 2 wt.%, particle agglomeration occurs due to inter-particle bridges by reaction products, forming clustered structures that adversely affect rheological properties.

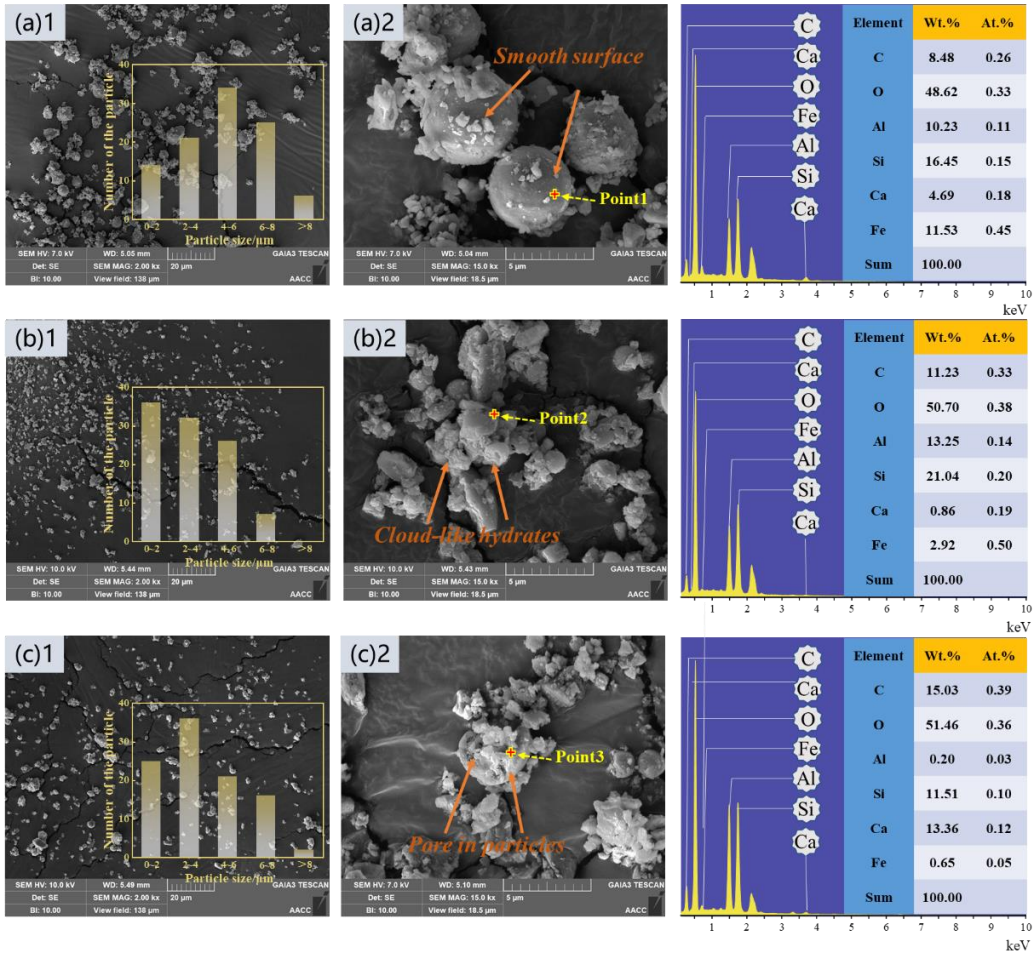

Fig. 15. SEM micrographs of (a) MF0, (b)MF2, (c)MF4.

3.3.3. BET analysis

Fig. 16 presents the specific surface area and pore volume characteristics of AA modified FA. The results also demonstrate a non-monotonic trend with AA dosages, exhibiting an initial increase followed by subsequent reduction. Optimal modification occurs at 2 wt.% AA dosage, where the specific surface area peaks at 8.57 m^2/g (representing a 20% enhancement compared to that of the unmodified reference) while the total pore volume increases from 0.0364 to 0.0382 cm^3/g. This enhancement correlates with microstructural modifications observed in Fig. 15, where AA treatment induces surface porosity through two primary mechanisms. (1) The reaction between $CaCO_3$ and AA forming calcium acetate, which creates in-situ pores and surface fractures. (2) The dispersion of newly formed phases across the particle surfaces. These findings align with one previous work [9] that reported similar surface area enhancement in phosphoric acid-treated steel slag systems. Beyond the optimal dosage (2 wt.% AA), both specific surface area and pore volume decrease significantly. This deterioration stems from excessive hydration product formation, which promotes particle bridging and agglomeration (Fig. 15), ultimately increasing effective particle size while reducing surface area and porosity.

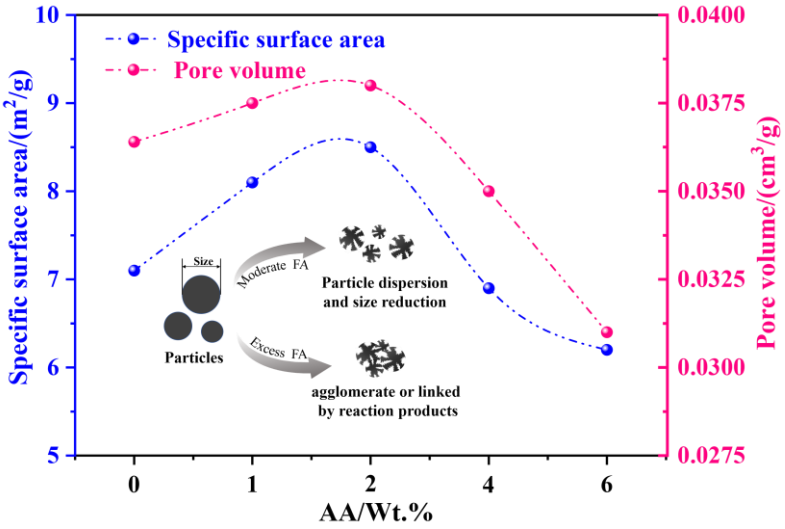

Fig. 16. Specific surface area and pore volume of AA modified FA.

3.4. Carbon footprint calculation and analysis

The carbon footprint serves as a critical metric for quantifying greenhouse gas emissions, enabling a comprehensive assessment of the environmental benefits. In this investigation, a life cycle assessment (LCA) framework was applied to evaluate the carbon emissions of three AFB variants. The system boundary for the AFB, as illustrated in Fig. 17, encompasses key stages including raw material extraction and transportation, product manufacturing, distribution logistics, and end-of-life waste recycling and reuse [38, 39]. Building upon this life cycle system, a computational model for AFB carbon emissions was derived, expressed mathematically in Eqs. (4)–(9).

$$C_e = M_1 \times CEF_{e1} + M_2 \times CEF_{e2} + M_3 \times CEF_{e3} + M_4 \times CEF_{e4} + M_5 \times CEF_{e5} + M_6 \times CEF_{e6} \quad (4)$$

$$C_t = (M_1 + M_2 + M_3 + M_4 + M_5 + M_6) \times S_{t1} \times CEF_{t1} + M_s \times S_{t2} \times CEF_{t2} \quad (5)$$

$$C_p = M_s \times CEF_p \quad (6)$$

$$C_r = M_1 \times CEF_{r1} + M_2 \times CEF_{r2} \quad (7)$$

$$C_a = M_s \times CO_{2\,uptake}(\%) \quad (8)$$

$$C = C_e + C_t + C_p + C_r + C_a \quad (9)$$

Where, C_e is the carbon emission during the introduction of raw materials, CO_2 equivalent; M_1, M_2, M_3, M_4, M_5, M_6 are the mass of FA, S, AA, NaOH, $Na_2O{\cdot}3.3SiO_2$ and water in the functional unit AFB, t; CEF_{e1}, CEF_{e2}, CEF_{e3}, CEF_{e4}, CEF_{e5}, CEF_{e6} are the carbon emission factors of FA, S, AA,

NaOH, $Na_2O·3.3SiO_2$ and water extraction stages, $KgCO_2eq·t^{-1}$; C_t is the total carbon emission of various raw materials, products and energy transportation, CO_2 equivalent; CEF_{t1} is the carbon emission factor in the raw material transportation stage, $KgCO_2eq·t^{-1}$; CEF_{t2} is the carbon emission factor in the AFB transportation stage, $KgCO_2eq·t^{-1}$; S_{t1} and S_{t2} are the raw material transportation distance and AFB transportation distance, km; M_s is the mass of the functional unit AFB, t; C_p is the total carbon emission generated in the product production process, CO_2 equivalent; CEF_p is the carbon emission factor in the AFB production stage, $KgCO_2eq·t^{-1}$; C_r is the carbon emission reduction from industrial solid waste recycling, which is a negative value, CO_2 equivalent; CEF_{r1} and CEF_{r2} are the carbon emission factors for FA and S recycling, respectively, which are negative values, $KgCO_2eq·t^{-1}$; C_a is the carbon emission reduction from CO_2 sequestration in the functional unit AFB, which is a negative value, CO_2 equivalent. C is the total carbon emission of the functional unit AFB, CO_2 equivalent.

The calculated carbon emissions for each AFB variant are listed in Table 6. The results indicate that the primary sources of emissions arise from raw material and product transportation. To mitigate this, optimizing logistical strategies—such as prioritizing local material procurement and reducing long-distance transport—is imperative. Notably, the total carbon emissions for AFB0(R), AFB0(C), and AFB1(C) were quantified as 67.95 kg/t, 47.50 kg/t, and -1.57 kg/t, respectively. Compared to AFB0(R), AFB0(C) exhibits a decrease of 20.45 kg/t in total emissions. Interestedly, at 1 wt.% AA dosage, AFB1(C) demonstrates a substantial decrease of 69.52 kg/t relative to AFB1(R), underscoring the efficacy of AA incorporation in significantly lowering carbon emissions. In the broader context, China's annual CO_2 emissions reached 12.6 billion t in 2023, with coal mining generating approximately 3.3 billion m^3 of goaf space [40]. Scenario-based extrapolation suggests that sealing the goaf with AFB could sequester 3.05 million t of CO_2 over the lifecycle of the material, presenting a viable strategy to enhance carbon capture, utilization, and storage (CCUS) implementation in mining sectors.

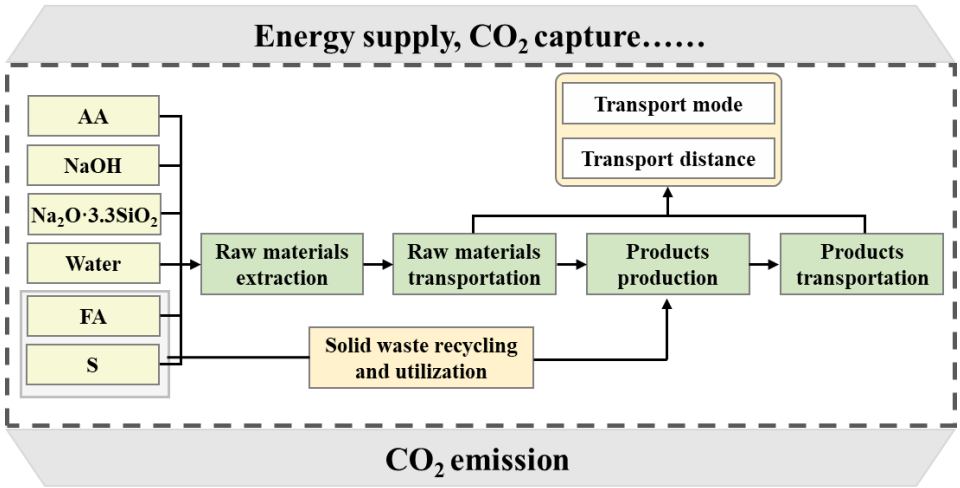

Fig. 17. LCA boundary of AFB.

Table 6. Calculation results of carbon emissions, kg/t.

Number	C_e	C_t	C_p	C_r	C_a	C
AFB0(R)	46.28	98.53	1.74	-78.60	0	67.95
AFB0(C)	46.28	98.53	1.74	-78.60	-20.45	47.50
AFB1(C)	49.37	98.62	1.75	-78.60	-72.71	-1.57

4. Discussion

The CO_2 sequestration mechanism of AFB comprises two pathways: (1) chemical sequestration via mineralization reactions and (2) physical sequestration through pore and surface adsorption. The physical CO_2 sequestration capacity was quantified by subtracting the chemically sequestered CO_2 (determined via thermal mass loss analysis, Section 3.2.2) from the total CO_2 uptake (measured gravimetrically, Section 3.1.1), as illustrated in Fig. 18. Furthermore, Fig. 19 reveals the evolution of AFB's microstructure and its correlation with CO_2 sequestration efficiency across varying AA dosages, providing mechanistic insights into the material's carbon capture performance.

Microstructural analysis of the AFB0 sample (Fig. 19a) reveals that carbonation-induced agglomeration of FA particles significantly impairs slurry rheology. This observation aligns with previous studies by Monkman et al. [41] and Huo et al. [42], demonstrating that increased CO_2 sequestration correlates with decreased slurry fluidity due to calcium carbonate precipitation. The introduction of AA-modified FA induces substantial microstructural reorganization. At 2 wt.% AA dosage (Fig. 19c), modified FA particles exhibit decreased particle size and enhanced surface roughness, facilitating greater carbonate formation. Notably, AA incorporation generates surface-bound fluffy structures that function as both dispersants and lubricants, yielding smaller particle clusters and improved slurry homogeneity. However, excessive AA addition (Fig. 19d) promotes particle bridging through undesirable AA-FA reactions, ultimately forming large aggregates that degrade rheological performance.

To highlight the AA modification, mechanical grinding refines FA particles and expands specific surface area to boost carbon sequestration, yet excessive particle fining sharply elevates slurry yield stress and impairs flowability after carbon mineralization [43]. Strong inorganic acid etching boosts mineral reactivity but neutralizes alkaline activators and generates insoluble phosphate precipitates that block pore channels for CO_2 adsorption [44]. Conventional surfactants only optimize fresh slurry rheology via electrostatic and steric repulsion, without improving the intrinsic calcium leaching and carbon fixation potential of raw FA precursors [45]. In contrast, acetic acid coupled mechanical milling achieves synergistic dual regulation of carbon capture and workability: mild organic acid etching

continuously releases Ca^{2+} to sustain cyclic CO_2 mineralization, while adsorbed acetate groups act as interfacial lubricants to offset rheological deterioration induced by carbonate precipitation [46]. Excess AA triggers particle bridging via calcium acetate crystals, and blending trace low dosage surfactants is proposed to mitigate this adverse effect in follow up optimization. Proton-donating organic mediators could significantly boost Ca^{2+} leaching from alkaline solid waste; dissolved Ca^{2+} forms soluble acetate complexes and avoids early passivation by hydroxide precipitates, thereby improving subsequent CO_2 mineralization efficiency [47]. Acetate-based extractants effectively extract utilizable calcium from calcium-rich alkaline residues, and crystalline calcium-acetate phases can be detected by XRD under high-dosage acetate treatment conditions [48]. Organic-acid-mediated indirect mineralization relies heavily on the reversible complexation between acetate anions and Ca^{2+} to break silicate-glass passivation layers and regulate Ca-speciation distribution between solid and liquid phases [49, 50]. In our XRD results of modified FA (Fig.14), new diffraction peaks corresponding to calcium acetate emerged under excessive AA dosage (>2 wt.%), which serves as solid-phase circumstantial evidence for calcium-acetate formation.

For practical engineering deployment, multi-objective indicators including CO_2 sequestration capacity, yield stress, plastic viscosity, thixotropy, flowability and carbon footprint should be jointly evaluated rather than relying only on the single maximum CO_2 uptake value. The 1 wt.% AA modified sample obtains the highest CO_2 sequestration, yet its relatively high yield stress increases pipeline pumping difficulty. By comparison, 2 wt.% AA modification retains favorable carbon-fixing performance and achieves the minimum yield stress, plastic viscosity and thixotropic hysteresis-loop area, which is more favorable for on-site mine backfill construction. Nevertheless, it should be noted that acetic acid itself carries environmental burdens originating from its manufacturing, logistics and on-site handling; residual acetate and calcium acetate within hardened backfill may also introduce overlooked environmental risks, which deserve further incorporation into future life-cycle evaluation frameworks.

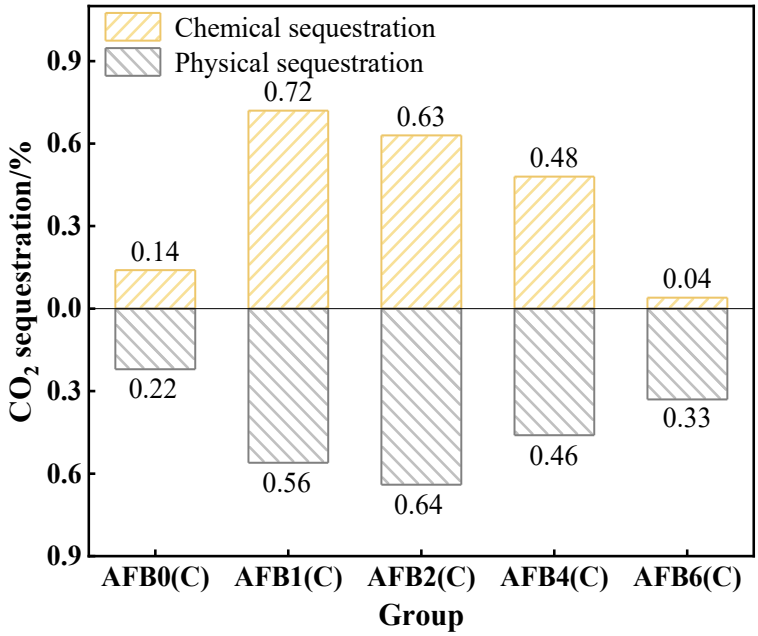

Fig. 18. AFB physical and chemical CO_2 sequestration capacity.

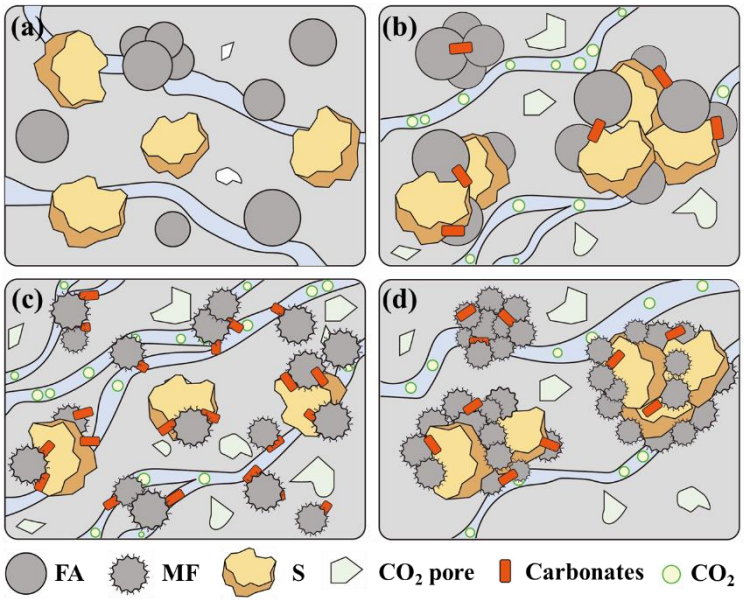

Fig. 19. AFB microstructure and CO_2 sequestration schematic, (a)AFB0(R), (b)AFB0(C), (c)AFB2(C) and (d)AFB4(C).

5. Conclusion

This study systematically investigated the effect of AA modified FA on both CO_2 sequestration capacity and rheological properties of AFB. The underlying microstructural evolution mechanisms were also elucidated. The principal findings are summarized as follows:

(1) CO_2 sequestration in AFB relies on two pathways, one is physical adsorption on particle surfaces and pores, and the other is chemical mineralization reactions. AA dosage affects carbon capture efficiency in a non-monotonical way. The maximum CO_2 uptake of 1.28% is obtained at 1 wt.% AA.

(2) Carbonation degrades the rheological performance of unmodified AFB. AA modification significantly improves slurry flow property. Although 1 wt.% AA yields the maximum CO_2-sequestration capacity, 2 wt.% AA provides the best rheological indices (yield stress: 9.28 Pa; plastic viscosity: 0.67 Pa·s; hysteresis loop area: 144.05 Pa/s) while maintaining comparable high CO_2-uptake. Considering the practical pipeline-pumping requirement for mine backfill, 2 wt.% AA is selected as the comprehensive optimum formulation.

(3) Microstructural analysis reveals that AA modification induces three key effects: (i) particle size reduction of FA, (ii) generation of in-situ surface porosity, and (iii) formation of dispersive/lubricative surface phases. These modifications collectively increase the specific surface area for carbonate formation while simultaneously improving slurry workability.

(4) Life cycle assessment demonstrates that AA addition substantially reduces the carbon footprint of AFB production. The modified formulation achieves net-negative carbon emissions across its lifecycle, representing a promising solution for sustainable mine backfilling applications.

Acknowledgements

The authors would like to thank the support from the National Key R&D Program of China (2023YFC3904300), the National Natural Science Foundation of China (52304160), the Jiangsu Funding Program for Excellent Postdoctoral Talent (2022ZB524) and the Guizhou Province Science and Technology Project (XKBP[2025]019).

Data availability

Data will be made available on request.

Declaration of competing interest

The authors declare that they have no known competing financial interests or personal relationships that could have appeared to influence the work reported in this paper.

Author contribution statement

Binbin Huo: Conceptualization, Methodology, Investigation, Data curation, Formal analysis, Software, Visualization, Writing – original draft, Writing – review & editing. **Jixiong Zhang**:

Conceptualization, Methodology, Resources, Supervision, Project administration, Funding acquisition, Writing – review & editing. **Nan Zhou**: Investigation, Formal analysis, Validation, Writing – review & editing. **Meng Li**: Formal analysis, Validation, Writing – review & editing. **Qiang Guo**: Methodology, Validation, Writing – review & editing. **Manti Tan**: Methodology, Validation, Writing – review & editing. **Yifan Zhang**: Methodology, Validation, Writing – review & editing. **Xiao Wang**: Methodology, Validation, Resources, Supervision, Writing – review & editing. All authors have read and approved the final manuscript and agree to be accountable for all aspects of the work.

Use of AI statement

None.

References

[1] Li, B., Ma, J., Long, K., et al. CO_2 mineralization with fly ash for underground carbon-negative backfill. Journal of CO_2 Utilization, **2026**, 106: 103366. https://doi.org/10.1016/j.jcou.2026.103366.

[2] Gao, X., Xie, W., Yuan, K., et al. Mechanical properties and microstructural evolution of fly ash stabilized loess: Insights from multiscale analysis and environmental impacts. Environmental Technology & Innovation, **2026**, 41: 104729. https://doi.org/10.1016/j.jeti.2025.104729.

[3] Ding, T., He, J., Zheng, Y., et al. High-value recycling of industrial solid wastes using mineral carbonation: A review of recent developments. Materials Reports: Solidwaste and Ecomaterials, **2026**, 2: 9520022. https://doi.org/10.26599/MRSE.2026.9520001.

[4] Kuźnia, M. A Review of Coal Fly Ash Utilization: Environmental, Energy, and Material Assessment. Energies, **2025**, 18(1): 52. https://doi.org/10.3390/en18010052.

[5] Shi, Q., Zhu, Y., Deng, C., et al. Properties of ultrasound-assisted calcium ion leaching of fly ash for CO_2 mineralization. Separation and Purification Technology, **2026**, 408: 139145. https://doi.org/10.1016/j.seppur.2026.139145.

[6] Hamada, H., Abed, F., Al-Sadoon, Z., et al. Enhancing pozzolanic activity of fly ash via dry and wet milling: A comparative study for sustainable construction material enhancement. Journal of CO_2 Utilization, **2024**, 83: 102811. https://doi.org/10.1016/j.jcou.2024.102811.

[7] Li, S., Huang, Y., Sun, J., et al. Mechanisms of concentration control alkali activated fly ash stabilized saline soil in seasonally frozen regions. Scientific Reports, **2025**, 15: 285. https://doi.org/10.1038/s41598-024-82628-9.

[8] Zhao, T., Hai, D., Bi, Z., et al. Mechanochemically modified fly ash for adsorption of flue gas heavy metals in MSW incineration plants. Fuel, **2026**, 405: 136615. https://doi.org/10.1016/j.fuel.2025.136615.

[9] Huo, B., Li, B., Huang, S., et al. Hydration and soundness properties of phosphoric acid modified

steel slag powder. Construction and Building Materials, **2020**, 254: 119319. https://doi.org/10.1016/j.conbuildmat.2020.119319.

[10] Wang, D., Wang, H., Shen, P., et al. Preparation, performances and hydration mechanism of high-entropy solid waste-based binders. Materials Reports: Solidwaste and Ecomaterials, **2025**, 1: 9520015. https://doi.org/10.26599/MRSE.2025.9520015.

[11] Zhao, Y., Han, Y., Xia, L., et al. Study on the flow properties of modified magnesium-coal-based solid waste carbon sequestration backfill materials. International Journal of Greenhouse Gas Control, **2025**, 146: 104443. https://doi.org/10.1016/j.ijggc.2025.104443.

[12] Zhang, J., Ye, H., Gao, X., et al. Adsorption and desorption of polycarboxylate ether superplasticizer in fresh cementitious materials blended with mineral admixtures. Journal of Materials Research and Technology, **2022**, 17: 1740–1751. https://doi.org/10.1016/j.jmrt.2022.01.145.

[13] Pan, Z., Wang, Y., Yang, H., et al. Printability and compressive strength of alkali-activated fly ash-GGBFS-steel slag materials: effect of FA:GGBFS ratio and activator modulus. Journal of Building Engineering, **2026**, 128: 116405. https://doi.org/10.1016/j.jobe.2026.116405.

[14] Cao, X., Lyu, H., Chen, Y., et al. CO_2 nanobubble-enhanced cement–fly ash backfill: Optimizing aggregate gradation and microstructure. International Journal of Minerals, Metallurgy and Materials, **2026**, 33: 129–140. https://doi.org/10.1007/s12613-025-3154-2.

[15] Rong, N., Wang, Y., Wang, G., et al. Optimized acid leaching synthesis and steam regeneration of the steel slag derived calcium-based CO_2 capture sorbent. Journal of Cleaner Production, **2025**, 488: 144673. https://doi.org/10.1016/j.jclepro.2025.144673.

[16] Bao, W., Li, H., Zhang, Y. Selective leaching of steelmaking slag for indirect CO_2 mineral sequestration. Industrial & Engineering Chemistry Research, **2010**, 49: 2055-2063. https://doi.org/10.1021/ie801850s.

[17] Guo, Q., Huo, B., Yu, K., et al. Using acetic acid as a preconditioner to optimize rheology of alkali-activated coal gasification slag based backfill pastes. Minerals Engineering, **2024**, 218: 109040. https://doi.org/10.1016/j.mineng.2024.109040.

[18] Wang, H., Duan, Y. Mechanical Transformation of Fly Ash toward Its Utilization in Cemented Paste Backfill. Advances in Civil Engineering, **2021**, 2021: 5492272. https://doi.org/10.1155/2021/5492272.

[19] Huo, B., Zhang, Y., Wang, D. Optimizing CO_2 capture property of alkali-activated ladle slag materials with sodium dodecyl sulfate. Powder Technology, **2025**, 449: 120388. https://doi.org/10.1016/j.powtec.2024.120388.

[20] Guo, Y., Zhang, J., Long, K., et al. Experimental study on CO_2 sequestration capacity and mechanical characteristics evolution of solid wastes based carbon-negative backfill materials. Construction and Building Materials, **2024**, 440: 137457. https://doi.org/10.1016/j.conbuildmat.2024.137457.

[21] Tan, M., Li, X., Feng, Y., et al. Fly ash-derived mesoporous silica with large pore volume for augmented CO_2 capture. Fuel, **2023**, 351: 128874. https://doi.org/10.1016/j.fuel.2023.128874

[22] Shao, C., Liu, L., Zhang, X., et al. Influence of internal and external factors on the fluidity of modified magnesium slag-based backfill materials. Journal of Environmental Chemical Engineering, **2024**, 12: 111867. https://doi.org/10.1016/j.jece.2023.111867.

[23] Song, K., Kim, W., Park, S., et al. Preparation of Silica-Alumina Nanoparticles via Blast-Furnace Slag Dissolution in Low-Concentration Acetic Acid for Carbonation. Minerals, **2017**, 7(11): 206. https://doi.org/10.3390/min7110206.

[24] Yang, X., Wu, Y., Sun, K., et al. The Leaching Performance and Mechanism of Calcium Ions from Coal Fly Ash Under Sequential Alkaline-Acid Processing. Processes, **2026**, 14(11): 1731. https://doi.org/10.3390/pr14111731.

[25] Zhang, X., Liu, S., Wu, K., et al. Macroscopic behavior and microscopic structure of serpentine-MgO carbon sequestration foamed concrete. Journal of Building Engineering, **2024**, 86: 108962. https://doi.org/10.1016/j.jobe.2024.108962.

[26] Xu, W., Tian, M., Li, Q. Time-dependent rheological properties and mechanical performance of fresh cemented tailings backfill containing flocculants. Minerals Engineering, **2020**, 145: 106064. https://doi.org/10.1016/j.mineng.2019.106064.

[27] Xie, G., Liu, L., Suo, Y., et al. Influence of temperature effect on properties of modified magnesium slag-based low-carbon paste backfill materials. Construction and Building Materials, **2024**, 411: 134800. https://doi.org/10.1016/j.conbuildmat.2023.134800.

[28] Zhang, Y., Luo, X., Kong, X., et al. Rheological properties and microstructure of fresh cement pastes with varied dispersion media and superplasticizers. Powder Technology, **2018**, 330: 219-27. https://doi.org/10.1016/j.powtec.2018.02.014.

[29] Fang, K., Zhang, D., Wang, D., et al. The impact of coal gasification slag powder on fluidity, rheology and viscoelasticity properties of fresh cement paste. Journal of Building Engineering, **2023**, 69: 106237. https://doi.org/10.1016/j.jobe.2023.106237.

[30] Deng, X., Klein, B., Zhang, J., et al. Time-dependent rheological behaviour of cemented backfill mixture. International Journal of Mining, Reclamation and Environment, **2018**, 32: 145-62. https://doi.org/10.1080/17480930.2016.1239305.

[31] Fan, C., Wei, R., Cheng, T., et al. The positive contributions of steel slag in reducing carbon dioxide emissions in the steel industry: Waste heat recovery, carbon sequestration, and resource utilization. Chemical Engineering Journal, **2024**, 498: 155379. https://doi.org/10.1016/j.cej.2024.155379.

[32] Huo, B., Zhang, Q., Li, M., et al. Using recycled gangue to capture CO_2 and prepare alkali-activated backfill paste: Adsorption and microevolution mechanisms. Fuel, **2024**, 358: 130194. https://doi.org/10.1016/j.fuel.2023.130194.

[33] Liu, H., Zheng, Z., Yang, Q. Analysis of rheological characteristics of cement mortar based on

microstructure. International Journal of Materials and Product Technology, **2022**, 64: 211-21. https://doi.org/10.1504/IJMPT.2022.122886.

[34] Qin, L., Lin, S., Lin, H., et al. Characteristics of alkali-activated fly Ash-CO_2 mineralization reaction and micro carbon sequestration mechanism. International Journal of Greenhouse Gas Control, **2025**, 144: 104377. https://doi.org/10.1016/j.ijggc.2025.104377.

[35] Qin, L., Gao, X., Chen, T. Influence of mineral admixtures on carbonation curing of cement paste. Construction and Building Materials, **2019**, 212: 653-62. https://doi.org/10.1016/j.conbuildmat.2019.04.033.

[36] Lu, B., He, P., Liu, J., et al. Microstructure of Portland cement paste subjected to different CO_2 concentrations and further water curing. Journal of CO_2 Utilization, **2021**, 53: 101714. https://doi.org/10.1016/j.jcou.2021.101714.

[37] Ma, Y., Li, W., Jin, M., et al. Influences of leaching on the composition, structure and morphology of calcium silicate hydrate (C-S-H) with different Ca/Si ratios. Journal of Building Engineering, **2022**, 58: 105017. https://doi.org/10.1016/j.jobe.2022.105017.

[38] Saravanan, A., Karishma, S., Senthil Kumar, P., et al. A review on regeneration of biowaste into bio-products and bioenergy: Life cycle assessment and circular economy. Fuel, **2023**, 338: 127221. https://doi.org/10.1016/j.fuel.2022.127221.

[39] Hoo, D., Tang, S., Kikuchi, Y., et al. Prospective life cycle assessment: Identifying the most promising methods for sustainable cellulose nanocrystal production. Chemical Engineering Journal, **2024**, 498: 154964. https://doi.org/10.1016/j.cej.2024.154964.

[40] Yan, H., Shi, P., Zhang, J., et al. Mineralized carbon sequestration evaluation of coal-based solid waste consolidated backfill: A novel data-driven approach. Fuel, **2024**, 378: 132913. https://doi.org/10.1016/j.fuel.2024.132913.

[41] Monkman, S., Hwang, S.D., Khayat, K. Rheology modification of flowable mortar with CO_2. Cement and Concrete Composites, **2024**, 151: 105584. https://doi.org/10.1016/j.cemconcomp.2024.105584.

[42] Huo, B., Zhang, J., Zhou, N., et al. Effect of sodium dodecyl sulfate on the CO_2 sequestration and rheological properties of alkali-activated coal gasification slag backfill pastes. Journal of Mining and Safety Engineering, **2024**, 41: 1279-1288. http://ckxb.cumt.edu.cn/CN/10.13545/j.cnki.jmse.2024.0433.

[43] Liu, H., Ren, S., Xu, C., et al. Influence of different grinding degrees of fly ash on geopolymer reaction characteristics. PLOS ONE, **2023**, 18(3): e0282927. https://doi.org/10.1371/journal.pone.0282927.

[44] Huo, M., Huang, C., Guo, A., et al. From waste to functional materials: advances in porous material synthesis derived from coal gasification slag. RSC Advances, **2025**, 15(30): 18893−18909. https://doi.org/10.1039/d5ra02243f.

[45] Han, F., Wu, S., Ding, H., et al. Adsorption Capacity Enhancement on Coal Fly Ash for Carbon

Capture in Humid Flue Gas: A Critical Review. Energy & Fuels, **2025**, 39(23): 10768−10801. https://doi.org/10.1021/acs.energyfuels.5c01124.

[46] Sukkathanyawat, H., Bampenrat, A., Jarunglumlert, T., et al. Modification of waste sugarcane bagasse fly for CO_2 capture application. Materials for Renewable and Sustainable Energy, **2022**, 11: 267–276. https://doi.org/10.1007/s40243-022-00219-y.

[47] Zhang, Y., Zhan, G., Huang, Z., et al. Performance and mechanisms of alkaline solid waste in CO_2 mineralization and utilization. Waste Management, **2024**, 175(2024): 62-72. https://doi.org/10.1016/j.wasman.2023.12.047.

[48] Ma, Y., Zhang, X., Du, Z., et al. Research on utilizable calcium from calcium carbide slag with different extractors and its effect on CO_2 mineralization. Materials, **2024**, 17(5): 1068. https://doi.org/10.3390/ma17051068.

[49] Zajac, M., Dienemann, W., Skocek, J. Circular concrete: Sustainable practices through recycling and CO_2 mineralization. Materials Reports: Solidwaste and Ecomaterials, **2025**, 1: 9520016. https://doi.org/10.26599/MRSE.2025.9520016.

[50] Walker, I., Bell, R., Rippy, K. Mineralization of alkaline waste for CCUS. npj Materials Sustainability, **2024**, 2(1): 28. https://doi.org/10.1038/s44296-024-00031-x.

Author biography

Binbin Huo, Associate Professor at China University of Mining and Technology, primarily engages in research on solid waste resource utilization and mining functional materials.

Jixiong Zhang, Professor and President of China University of Mining and Technology. He is a recipient of the National Science Fund for Distinguished Young Scholars. His primary research focuses on backfill mining.

Xiao Wang, Lecturer at Xuzhou University of Technology. Her primary research focuses on environmental functional materials.